

# Topology optimization of flexoelectric metamaterials with apparent piezoelectricity

F. Greco<sup>1</sup>, D. Codony<sup>2,1</sup>, H. Mohammadi<sup>3</sup>, S. Fernández-Méndez<sup>1</sup>, I. Arias<sup>1,3\*</sup>

<sup>1</sup> Laboratori de Càlcul Numèric (LaCàN), Universitat Politècnica de Catalunya (UPC), Campus Nord UPC-C2, E-08034 Barcelona, Spain

<sup>2</sup> College of Engineering, Georgia Institute of Technology, Atlanta, GA 30332, USA,

<sup>3</sup> Centre Internacional de Mètodes Numèrics en Enginyeria (CIMNE), 08034 Barcelona, Spain

\* Corresponding author; E-mail: irene.arias@upc.edu.

## Abstract

The flexoelectric effect, coupling polarization and strain gradient as well as strain and electric field gradients, is universal to dielectrics, but, as compared to piezoelectricity, it is more difficult to harness as it requires field gradients and it is a small-scale effect. These drawbacks can be overcome by suitably designing metamaterials made of a non-piezoelectric base material but exhibiting apparent piezoelectricity. We develop a theoretical and computational framework to perform topology optimization of the representative volume element of such metamaterials by accurately modeling the governing equations of flexoelectricity using a Cartesian B-spline method, describing geometry with a level set, and resorting to genetic algorithms for optimization. We consider a multi-objective optimization problem where area fraction competes with four fundamental piezoelectric functionalities (stress/strain sensor/actuator). We computationally obtain Pareto fronts, and discuss the different geometries depending on the apparent piezoelectric coefficient being optimized. In general, we find competitive estimations of apparent piezoelectricity as compared to reference materials such as quartz and PZT ceramics. This opens the possibility to design devices for sensing, actuation and energy harvesting from a much wider, cheaper and effective class of materials.

*Keywords:* metamaterials, piezoelectricity, flexoelectricity, dielectric materials, genetic algorithms

## 1 Introduction

The property of some materials to transduce electrical fields into mechanical deformations and vice versa, known as piezoelectric effect (Martin, 1972), is crucial for the design of a variety of devices, such as sensors (Gautschi, 2006, Tressler et al., 1998), actuators (Gao et al., 2020, Sinha et al., 2009), energy harvesters (Erturk and Inman, 2011, Safaei et al., 2019) and microelectromechanical systems (Muralt, 2008, Smith et al., 2012). However, these material are in general lead-based, brittle and limited to be used in a specific temperature range (Haertling, 1999). Because of these limitations, there has been intense research over the last years to develop piezoelectricity in a broader class of lead-free materials (Hong et al., 2016, Rödel et al., 2009, Saito et al., 2004).

Besides material design at a molecular scale, an alternative idea is to achieve apparent piezoelectricity in metamaterials or composites made of non-piezoelectric constituents by an appropriate geometry or combination of materials (Fousek et al., 1999, Sharma et al., 2007). This can be achieved through flexoelectricity (Wang et al., 2019b), a coupling mechanism between strain gradient and electric polarization (direct flexoelectricity), or electric polarization gradient and strain (converse flexoelectricity). Unlike piezoelectricity which is only present in

non-centrosymmetric dielectrics, flexoelectricity is a property of all dielectric materials including crystals, polymers, biomaterials, liquid crystals, etc. (Jiang et al., 2013, Nguyen et al., 2013, Wang et al., 2019a, Zubko et al., 2013). As a result of a non-uniform deformation applied on a generic dielectric material and regardless of the symmetry of its microscopic structure, strain gradients break locally the spatial inversion symmetry inducing an electric response. The question of how to design a material such that local flexoelectric couplings result in significant apparent piezoelectricity is far from obvious.

In Mocci et al. (2021), we proposed a class of geometrically polarized architected dielectrics with apparent piezoelectricity. By considering periodic metamaterials made of non-piezoelectric flexoelectric materials, we showed that (1) geometric polarization (lack of geometric centrosymmetry) of the representative volume element (RVE) and (2) small-scale geometric features subjected to bending are enough to achieve an apparent piezoelectric behavior similar to that of Quartz and lead zirconium titanate (PZT) materials. Several designs were proposed out of physical reasoning and their geometric parameters varied, concluding that different piezoelectric coupling coefficients pertinent to different functionalities, e.g. strain/stress sensors or actuators (Ikeda, 1996, Mocci et al., 2021), require different designs. Here, the goal is to develop a systematic framework for the topology optimization of the flexoelectric unit cell of 2D apparently-piezoelectric metamaterials.

To accomplish this, we consider generalized periodic boundary conditions on an RVE, an optimization procedure based on genetic algorithms (GA) (Tomassini, 1995) and optimize for the four main apparent piezoelectric coupling coefficients (Ikeda, 1996, Mocci et al., 2021) pertinent to different piezoelectric applications. We approximate the system of fourth-order partial differential equations (PDE) using a direct Galerkin approach based on smooth uniform Cartesian B-spline basis functions. To describe the shape of the RVE, we resort to the level-set method to model the geometry and to an immersed boundary approach (Codony et al., 2019). Alternative methods to solve the flexoelectric PDE include  $C^1$  triangular elements (Yvonnet and Liu, 2017), mixed formulations (Deng et al., 2017, Mao et al., 2016), smooth meshfree schemes (Abdollahi et al., 2014, Zhuang et al., 2020), conforming isogeometric formulations (Codony et al., 2020, Do et al., 2019, Liu et al., 2019, Sharma et al., 2020, Thai et al., 2018) or a  $C^0$  interior penalty method (Balcells-Quintana et al., 2022, Ventura et al., 2021). The combination of immersed boundary Cartesian B-splines and level sets achieves conceptual simplicity, robustness, accuracy and the ability to easily perturb geometry during optimization. Gradient-based topology optimization with level sets requires smoothing algorithms and re-initializations to maintain the signed distance property for the numerical convergence (López et al., 2022). Despite the higher computational cost of GA, their implementation is straightforward, can be trivially parallelized, and are better suited for design space exploration for global minima. They have been successfully used in the topology optimization of mechanical structures (Coello and Christiansen, 2000, Erbatur et al., 2000, Hajela and Lee, 1995, Jenkins, 1991) and electromagnetic systems (Im et al., 2003).

Topology optimization has been applied previously to flexoelectric nanostructures (Ghasemi et al., 2017, 2018, Hamdia et al., 2019, López et al., 2022, Nanthakumar et al., 2017, Zhang et al., 2022), by means of level sets and mixed finite elements (Nanthakumar et al., 2017), isogeometric approximations and level sets (Ghasemi et al., 2017, 2018), a morphable void approach (Zhang et al., 2022), or a phase-field method with a diffuse boundary (López et al., 2022). Optimization algorithms include gradient methods, Monte Carlo algorithms (Hamdia et al., 2022), as well as deep learning approaches (Hamdia et al., 2019). These works focused on finite structures (beams

under bending and compressed blocks or pyramids) and optimized a ratio between mechanical and electric energy, rather than a direct measure of device performance for a given functionality. Interestingly, none of these approaches produce the kind of geometrically polarized microstructures proposed by [Mocci et al. \(2021\)](#). Instead, in the present work, the microstructural topology of architected materials is optimized for apparent piezoelectric performance and the resulting RVEs are reminiscent of those proposed by [Mocci et al. \(2021\)](#).

The outline of the paper is the following. We first formulate the flexoelectric problem into the representative volume element, then we discuss the numerical discretization and the level set geometry description; we also discuss how the GA are used and we introduce a framework to obtain valid material configurations; finally we show and discuss the results for the optimization of different apparent piezoelectric coefficients. Concluding remarks follow.

## 2 Formulation for flexoelectric representative volume element

We consider a periodic flexoelectric metamaterial, and choose the displacement field  $\mathbf{u}(\mathbf{x})$  and the electric potential  $\phi(\mathbf{x})$  as the primal variables characterizing it. In the following, repeated indices imply sum over spatial dimensions, and indices after a comma (,) denote the partial space derivative along that dimension. We formulate the differential problem within the unit cell, referred to as representative volume element (RVE), c.f. Fig. 1, as follows. The strong form of the boundary value problem in  $\Omega \subset \Omega^{\text{RVE}} = [0, L_x] \times [0, L_y]$  of a linear Lifshitz-invariant ([Codony et al., 2021](#)) flexoelectric metamaterial is described next.

The constitutive relations for the linear flexoelectric material relate the stress tensor, electric displacement and their higher-order counterparts with the primal variables  $\mathbf{u}$ ,  $\phi$  and the material tensors as follows:

$$\hat{\sigma}_{ij}(\mathbf{u}, \phi) = C_{ijkl}\varepsilon_{kl}(\mathbf{u}) + \frac{1}{2}\mu_{lijk}E_{l,k}(\phi), \quad (1a)$$

$$\tilde{\sigma}_{ijk}(\mathbf{u}, \phi) = h_{ijklmn}\varepsilon_{lm,n}(\mathbf{u}) - \frac{1}{2}\mu_{lijk}E_l(\phi), \quad (1b)$$

$$\hat{D}_l(\mathbf{u}, \phi) = \epsilon_{lm}E_m(\phi) + \frac{1}{2}\mu_{lijk}\varepsilon_{ij,k}(\mathbf{u}), \quad (1c)$$

$$\tilde{D}_{kl}(\mathbf{u}, \phi) = M_{mnlk}E_{m,n}(\phi) - \frac{1}{2}\mu_{lijk}\varepsilon_{ij}(\mathbf{u}), \quad (1d)$$

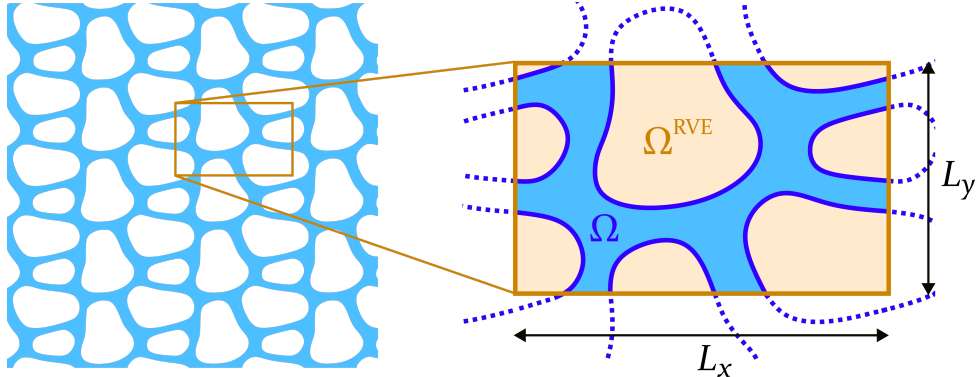


Figure 1: Architected metamaterial (left) and representative volume element (right).

where  $\varepsilon_{ij}(\mathbf{u}) = (u_{i,j} + u_{j,i})/2$  is the strain field,  $E_l(\phi) = -\phi_{,l}$  the electric field,  $C_{ijkl}$  the elasticity tensor (in terms of Young modulus  $Y$  and Poisson ratio  $\nu$ ),  $h_{ijklmn}$  the strain-gradient elasticity tensor (in terms of  $Y$ ,  $\nu$  and the mechanical length scale  $\ell_{\text{mech}}$ ),  $\epsilon_{lm}$  the dielectricity tensor (in terms of the dielectric permittivity  $\epsilon$ ),  $M_{mnlk}$  the gradient dielectricity tensor (in terms of  $\epsilon$  and the electrical length scale  $\ell_{\text{elec}}$ ) and  $\mu_{lijk}$  the flexoelectric tensor (in terms of the longitudinal  $\mu_L$ , transversal  $\mu_T$  and shear  $\mu_S$  flexoelectric coefficients). See details in Appendix A in [Codony et al. \(2021\)](#). The fourth-order Euler-Lagrange equations stating balance of linear momentum and Gauss's law for dielectrics are then

$$\hat{\sigma}_{ij,j}(\mathbf{u}, \phi) - \hat{\sigma}_{ijk,kj}(\mathbf{u}, \phi) = 0 \quad \text{in } \Omega, \quad (2a)$$

$$\hat{D}_{l,l}(\mathbf{u}, \phi) - \hat{D}_{lk,kl}(\mathbf{u}, \phi) = 0 \quad \text{in } \Omega, \quad (2b)$$

where we assume no volumetric external loads.

The components of the primal unknowns are  $\mathcal{C}^1$ -continuous in  $\Omega$  due to the high-order nature of the PDE system. The boundary of the domain  $\partial\Omega$  has two parts, the boundary of the RVE  $\partial\Omega^{\text{RVE}}$ , which is not an actual material boundary and is subjected to generalized periodicity conditions, and the physical part of the boundary  $\partial\Omega \setminus \partial\Omega^{\text{RVE}}$ . Homogeneous Neumann conditions are considered at every physical boundary in the RVE, i.e. there are no tractions  $\mathbf{t}$ , double tractions  $\mathbf{r}$ , edge forces  $\mathbf{j}$ , electric charges  $w$ , double electric charges  $\mathbf{r}$ , or edge charges  $\wp$  on the physical part of  $\partial\Omega$ . Mathematically,

$$\mathbf{t} = \mathbf{r} = \mathbf{j} = \mathbf{0}, \quad w = \mathbf{r} = \wp = 0 \quad \text{on } \partial\Omega \setminus \partial\Omega^{\text{RVE}}. \quad (3)$$

We refer to Ref. [Codony et al. \(2021\)](#) for a detailed description of the Neumann quantities involved in Eq. (3).

A common assumption in boundary value problems of periodic metamaterials is that the primal variables are *generalized-periodic* ([Balcells-Quintana et al., 2022](#), [Barceló-Mercader et al., 2023](#)), a procedure that allows us to consider macroscopic strains and electric fields at the level of the RVE. Generalized periodic conditions require that primal field gradients are periodic functions within the RVE, whereas the primal fields themselves (displacement and electric potential) are continuous across contiguous RVE modulo the jumps resulting from the macroscopic strain and electric fields. For second order PDE, these conditions also ensure that the interfaces between contiguous RVE are in equilibrium ([Barceló-Mercader et al., 2023](#)).

In the present paper, the fourth-order nature of the PDE requires the second gradient of the primal variables to be periodic as well, in order to ensure equilibrium at the RVE interfaces ([Barceló-Mercader et al., 2022](#), [Barceló-Mercader et al., 2023](#)). Hence, the displacement field  $\mathbf{u}(\mathbf{x})$  and the electric potential  $\phi(\mathbf{x})$  are restricted to be *high-order* generalized-periodic functions, with  $\mathcal{C}^1$ -continuous components. They can be expressed as

$$\mathbf{u}(\mathbf{x}) = \mathbf{u}^P(\mathbf{x}) + \overline{\mathbf{G}} \cdot \mathbf{x}, \quad (4a)$$

$$\phi(\mathbf{x}) = \phi^P(\mathbf{x}) - \overline{\mathbf{E}} \cdot \mathbf{x}. \quad (4b)$$

Hence, their gradients are

$$\mathbf{G}(\mathbf{x}) \equiv \nabla \mathbf{u}(\mathbf{x}) = \nabla \mathbf{u}^P(\mathbf{x}) + \overline{\mathbf{G}}, \quad (5a)$$

$$\mathbf{E}(\mathbf{x}) \equiv -\nabla \phi(\mathbf{x}) = -\nabla \phi^P(\mathbf{x}) + \overline{\mathbf{E}}. \quad (5b)$$

In the equations above,  $\mathbf{u}^P(\mathbf{x})$  and  $\phi^P(\mathbf{x})$  are periodic functions in  $\Omega^{\text{RVE}}$ , and represent the microscopic response of the material. The displacement gradient  $\mathbf{G}(\mathbf{x})$  and the electric field  $\mathbf{E}(\mathbf{x})$  are periodic functions as well. The quantities  $\bar{\mathbf{G}} \in \mathbb{R}^2 \times \mathbb{R}^2$  and  $\bar{\mathbf{E}} \in \mathbb{R}^2$  represent the macroscopic displacement and electric potential gradients, and are constant over  $\Omega^{\text{RVE}}$ . They are related to  $\mathbf{u}(\mathbf{x})$  and  $\phi(\mathbf{x})$  by the following equations:

$$\mathbf{u}(\xi = L_\xi) - \mathbf{u}(\xi = 0) = \mathbf{u}^P(\xi = L_\xi) + \bar{\mathbf{G}} \cdot \mathbf{e}_\xi L_\xi - \mathbf{u}^P(\xi = 0) = \bar{\mathbf{G}} \cdot \mathbf{e}_\xi L_\xi, \quad (6a)$$

$$\phi(\xi = L_\xi) - \phi(\xi = 0) = \phi^P(\xi = L_\xi) - \bar{\mathbf{E}} \cdot \mathbf{e}_\xi L_\xi - \phi^P(\xi = 0) = -\bar{\mathbf{E}} \cdot \mathbf{e}_\xi L_\xi, \quad (6b)$$

which imply

$$\bar{\mathbf{G}}(\mathbf{u}) = \begin{bmatrix} (\mathbf{u}_x(x = L_x) - \mathbf{u}_x(x = 0))/L_x & (\mathbf{u}_y(x = L_x) - \mathbf{u}_y(x = 0))/L_x \\ (\mathbf{u}_x(y = L_y) - \mathbf{u}_x(y = 0))/L_y & (\mathbf{u}_y(y = L_y) - \mathbf{u}_y(y = 0))/L_y \end{bmatrix}, \quad (7a)$$

$$\bar{\mathbf{E}}(\phi) = \begin{bmatrix} -(\phi(x = L_x) - \phi(x = 0))/L_x \\ -(\phi(y = L_y) - \phi(y = 0))/L_y \end{bmatrix}, \quad (7b)$$

where  $\xi = \{x, y\}$  and  $\mathbf{e}_\xi$  is the unit vector of the canonical basis along the  $\xi$ -direction.

Following Refs. Barceló-Mercader et al. (2022), Barceló-Mercader et al. (2023), the macroscopic gradient  $\bar{\mathbf{G}}(\mathbf{u})$  is decomposed in its symmetric ( $\bar{\boldsymbol{\varepsilon}}(\mathbf{u})$ ) and skew-symmetric ( $\bar{\mathbf{W}}(\mathbf{u})$ ) components, with

$$\bar{\boldsymbol{\varepsilon}}(\mathbf{u}) = (\bar{\mathbf{G}}(\mathbf{u}) + \bar{\mathbf{G}}(\mathbf{u})^T)/2, \quad (8a)$$

$$\bar{\mathbf{W}}(\mathbf{u}) = (\bar{\mathbf{G}}(\mathbf{u}) - \bar{\mathbf{G}}(\mathbf{u})^T)/2, \quad (8b)$$

where  $\bar{\boldsymbol{\varepsilon}}(\mathbf{u})$  is the macroscopic strain, and  $\bar{\mathbf{W}}(\mathbf{u})$  is the macroscopic infinitesimal rotation (spin), which corresponds to a rigid body motion and hence does not play any role in the Euler-Lagrange equations in (2). In the following, we choose to prevent a rigid body rotation by applying the condition

$$\bar{\mathbf{W}}(\mathbf{u}) = \mathbf{0} \quad \leftrightarrow \quad \bar{G}_{xy}(\mathbf{u}) = \bar{G}_{yx}(\mathbf{u}) \quad \leftrightarrow \quad \bar{\mathbf{G}}(\mathbf{u}) = \bar{\boldsymbol{\varepsilon}}(\mathbf{u}). \quad (9)$$

As shown in Refs. Barceló-Mercader et al. (2022), Barceló-Mercader et al. (2023), the weak formulation of the boundary value problem presented above is

$$\begin{aligned} \frac{1}{|\Omega^{\text{RVE}}|} \int_{\Omega} \left( \hat{\sigma}_{ij}(\mathbf{u}, \phi) \varepsilon_{ij}(\delta \mathbf{u}) - \hat{D}_l(\mathbf{u}, \phi) E_l(\delta \phi) + \tilde{\sigma}_{ijk}(\mathbf{u}, \phi) \varepsilon_{ij,k}(\delta \mathbf{u}) - \tilde{D}_{lm}(\mathbf{u}, \phi) E_{l,m}(\delta \phi) \right) d\Omega \\ = \bar{\sigma}_{ij}(\mathbf{u}, \phi) \bar{\varepsilon}_{ij}(\delta \mathbf{u}) - \bar{D}_l(\mathbf{u}, \phi) \bar{E}_l(\delta \phi), \end{aligned} \quad (10)$$

for every admissible  $\delta \mathbf{u}(\mathbf{x})$  and  $\delta \phi(\mathbf{x})$ , where  $|\Omega^{\text{RVE}}| = L_x L_y$  is the total volume of the RVE (including material and void phases), and  $\bar{\boldsymbol{\sigma}}$  and  $\bar{\mathbf{D}}$  are the macroscopic stress and macroscopic electric displacement, defined as the macroscopic averages of the microscopic Cauchy stress and local electric displacement over  $\Omega$ :

$$\bar{\sigma}_{ij}(\mathbf{u}, \phi) = \frac{1}{|\Omega^{\text{RVE}}|} \int_{\Omega} \hat{\sigma}_{ij}(\mathbf{u}, \phi) d\Omega, \quad \bar{D}_l(\mathbf{u}, \phi) = \frac{1}{|\Omega^{\text{RVE}}|} \int_{\Omega} \hat{D}_l(\mathbf{u}, \phi) d\Omega. \quad (11)$$

The weak form in Eq. (10) is complemented with either Dirichlet or Neumann *macroscopic* conditions on each of the components of the macroscopic energy-conjugate variables  $\bar{\boldsymbol{\varepsilon}} - \bar{\boldsymbol{\sigma}}$  and

$\bar{\mathbf{E}} - \bar{\mathbf{D}}$ . Since homogeneous Neumann boundary conditions in Eq. (3) are enforced on every physical boundary in the RVE, the primal variables  $\mathbf{u}(\mathbf{x})$ ,  $\phi(\mathbf{x})$  are well-defined up to rigid body translations. In order to obtain a unique solution, it is sufficient imposing vanishing displacement and electric potential at an arbitrary point in  $\Omega$ .

The variations  $\delta\mathbf{u}(\mathbf{x})$  and  $\delta\phi(\mathbf{x})$  in Eq. (10) are high-order generalized-periodic functions with the same regularity as the primal unknowns  $\mathbf{u}(\mathbf{x})$  and  $\phi(\mathbf{x})$ , that is, their components are  $\mathcal{C}^1$ -continuous in  $\Omega$ . Hence, they can be expressed in terms of two independent sets of variations as

$$\delta\mathbf{u}(\mathbf{x}) = \delta\mathbf{u}^P(\mathbf{x}) + \bar{\boldsymbol{\varepsilon}}(\delta\mathbf{u}) \cdot \mathbf{x}, \quad (12a)$$

$$\delta\phi(\mathbf{x}) = \delta\phi^P(\mathbf{x}) - \bar{\mathbf{E}}(\delta\phi) \cdot \mathbf{x}, \quad (12b)$$

where the microscopic variations  $\delta\mathbf{u}^P(\mathbf{x})$  and  $\delta\phi^P(\mathbf{x})$  are high-order periodic functions with  $\mathcal{C}^1$ -continuous components in  $\Omega$ , and the macroscopic variations  $\bar{\boldsymbol{\varepsilon}}(\delta\mathbf{u})$  and  $\bar{\mathbf{E}}(\delta\phi)$  are constant functions whose components associated to macroscopic Dirichlet conditions are vanished.

### 3 Numerical discretization and level-set geometry description

Following the framework introduced by [Codony et al. \(2019\)](#), we consider a representation of the displacement and potential fields with uniform Cartesian B-spline basis functions ([de Boor, 2001](#), [Piegl and Tiller, 2012](#), [Rogers, 2001](#)), which are element-wise multivariate polynomial bases of degree  $p$  with  $\mathcal{C}^{p-1}$  continuity across elements. In order to fulfill the high-order generalized periodicity constraint in  $\Omega$ , we simply transform the uniform B-spline approximation space to a high-order generalized-periodic B-spline approximation space ([Barceló-Mercader et al., 2023](#)) by enforcing certain linear constraints on the basis functions intersecting the unit cell boundaries.

The resulting approximation space is a uniform Cartesian mesh with element sizes  $(h_x, h_y)$ , due to the tensor product nature of the basis functions. The element sizes  $h_\xi$  are a subdivision of the unit cell sizes  $L_\xi$ , so that  $L_\xi = n_\xi h_\xi$ , where  $n_\xi \in \mathbb{N}$  are the number of elements in each direction (taking periodicity into account) and  $\xi = \{x, y\}$ . The approximation space is spanned by two kind of basis functions, illustrated in Fig. 2: i) periodic multivariate B-spline functions with support on  $(p+1) \times (p+1)$  elements, which form a *high-order periodic* space, and ii) smooth ramp functions with support on  $(p+1) \times n_\xi$  elements and varying along one dimension only, which make the approximation space *generalized-periodic*. Every basis function inherits the  $\mathcal{C}^{p-1}$  continuity of the original uniform B-spline approximation space of degree  $p$ .

Mathematically, the unknowns of the problem  $\mathbf{u}(\mathbf{x})$  and  $\phi(\mathbf{x})$  are approximated as

$$[\mathbf{u}(\mathbf{x})]_\xi \approx [\mathbf{u}^h(\mathbf{x})]_\xi = N_i(\mathbf{x}) a_{i\xi}^u, \quad (13a)$$

$$\phi(\mathbf{x}) \approx \phi^h(\mathbf{x}) = N_i(\mathbf{x}) a_i^\phi, \quad (13b)$$

where  $N_i(\mathbf{x})$  are the basis functions in physical space and  $\{\mathbf{a}^u, \mathbf{a}^\phi\}$  are the degrees of freedom of  $\mathbf{u}^h$  and  $\phi^h$ .

The mesh is generally unfitted to  $\Omega$ , which can have an arbitrary shape. Some mesh elements are arbitrarily cut by  $\partial\Omega$ , and an appropriate strategy has to be implemented for their numerical integration and stabilization. In this work, we adopt an implicit description of the geometry  $\Omega$  by means of a level-set function, combined with a non-conforming quadtree numerical integration scheme ([Rank et al., 2012](#)). This approach leads to a simple implementation and a relatively

low computational cost. In order to alleviate severe ill-conditioning of the resulting algebraic system of equations due to cut cells, we consider the extended B-spline algorithm (Höllig et al., 2001), which consists on modifying the approximation space near  $\partial\Omega$  by binding basis functions whose support is mostly outside of  $\Omega$  with adjacent basis functions. See Refs. Codony et al. (2021, 2019) for further details.

The level-set function  $\Phi(\mathbf{x})$  is constructed from a linear combination of certain basis functions  $M(\mathbf{x})$  and coefficients  $\Phi$ , and the zero level of  $\Phi(\mathbf{x})$  describes the physical boundary of the domain  $\Omega$ . Mathematically,

$$\Omega = \{\mathbf{x} \in \Omega^{\text{RVE}} \mid \Phi(\mathbf{x}) > 0\}, \quad \text{where} \quad \Phi(\mathbf{x}) = M_i(\mathbf{x})\Phi_i. \quad (14)$$

The level set function  $\Phi(\mathbf{x})$  inherits the periodicity requirements on  $\Omega$ . Therefore, the basis functions  $M(\mathbf{x})$  must be periodic as well. In the present context, the simplest choice is to consider high-order multivariate periodic B-spline basis, which will generate a smooth boundary of  $\Omega$ . Note that  $M(\mathbf{x})$  span a periodic space (geometry space), whereas  $N(\mathbf{x})$  span a generalized-periodic one (computational space). Both sets of basis functions are independent and, in particular, it is of practical interest them having different resolutions, i.e. different “element” sizes. We typically consider a finer computational space than the geometry space, which has element sizes  $\ell_\xi \geq h_\xi$ . Specifically, in order to exploit the advantages of the presented numerical scheme, we restrict ourselves to a computational mesh constructed as a subdivision of the geometry mesh, in such a way that  $(\ell_x, \ell_y) = (s_x h_x, s_y h_y)$ , where  $s_\xi \in \mathbb{N}$  are the number of subdivisions in each direction. Note that  $\ell_\xi$  have to be also a subdivision of the unit cell sizes, so that the number of elements per dimension in the geometry mesh is  $n_\xi/s_\xi \in \mathbb{N}$ . Having a nested hierarchy of computational and geometry meshes allows us to consider just  $s_x \times s_y$

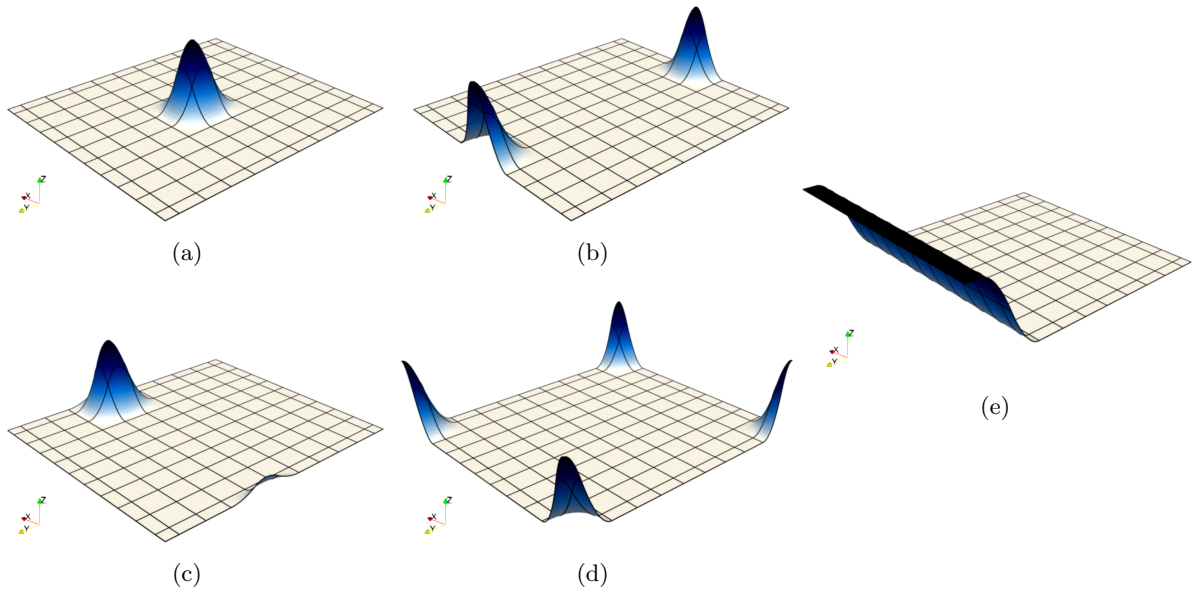


Figure 2: Some of the basis functions  $N_i(\mathbf{x})$  of degree  $p = 2$  spanning the high-order generalized-periodic approximation space on the computational mesh. (a)–(d) are periodic multivariate B-spline functions, whereas (e) is a smooth univariate ramp function.

reference elements for the evaluation of the level set function at the integration points of the quad-tree scheme in the computational mesh elements. This enables a very efficient strategy to classify elements in the computational mesh depending whether they are within  $\Omega$ , outside  $\Omega$ , or cut by  $\partial\Omega$ , a step that is required in any unfitted discretization method, as well as an efficient evaluation of the weak form at the integration points.

For a fixed geometry  $\Omega$  given by a set of coefficients  $\Phi$ , the weak form described in Section 2 is discretized on the computational mesh, by assembling the different contributions from interior and cut elements. The macroscopic Dirichlet conditions are enforced strongly by prescribing the degrees of freedom that multiply the corresponding ramp basis functions. As a result, an algebraic linear system of equations is obtained as

$$\mathbf{K}(\Phi) \cdot \mathbf{a}(\Phi) = \mathbf{f}(\Phi), \quad (15)$$

which one can solve to obtain  $\mathbf{a}(\Phi)$ , and therefore the approximated solution fields.

### 3.1 Identifying valid level set configurations

As we can observe in Fig. 3, a randomly generated level set description of  $\Omega$  yields domains with disconnected parts in general. However, valid topologies for architected materials require fully connected domains. To this end, the following algorithm is used to identify the number of connected parts or groups  $N_g$  present in the structure:

- the domain described by the level set is first sampled with a point cloud by considering a fixed tensor product grid in each level set element (Fig. 4a); that is, the level set function is evaluated on a regular grid and the points with  $\Phi(\mathbf{x}) \geq 0$  are maintained;
- the Delaunay triangulation is then constructed on this point cloud (Fig. 4b) and a shape containing the convex-hull of the cloud is obtained;
- the alpha shape criterion (Akkiraju et al., 1995) is used to extract an approximation of the shape of the domain. The idea of this method is to remove from the triangulation all the triangles whose circumradius is bigger than a fixed  $\alpha$  value, which in this case corresponds to the resolution used for the level set sampling;
- starting from the alpha-shape triangulation of the domain (Fig. 4c), the number of groups  $N_g$  is counted.

For this last step, it is convenient to convert the triangulation into a graph object in MATLAB<sup>®</sup>, *account for its periodicity by modifying its connectivity*, and use the `conncomp` function (Tarjan, 1972). To account for the periodicity of the RVE, the connectivity matrix of the triangulation is modified by identifying the vertices of the triangulation lying on the RVE boundaries and their periodic images with the same index. As an example, by naively counting the number of groups in Fig. 4d without taking periodicity into account,  $N_g = 4$  is obtained, indicating that the structure is disconnected. On the other hand, counting the number of groups with this updated connectivity matrix gives the correct assessment  $N_g = 1$  that indicates a globally connected structure.

However, having a number of groups  $N_g = 1$  in the RVE is not sufficient to assert that the periodic structure is actually connected. On top of that, it is also required that, for each point in the RVE, it is possible to create a path that connects this point with itself while intersecting

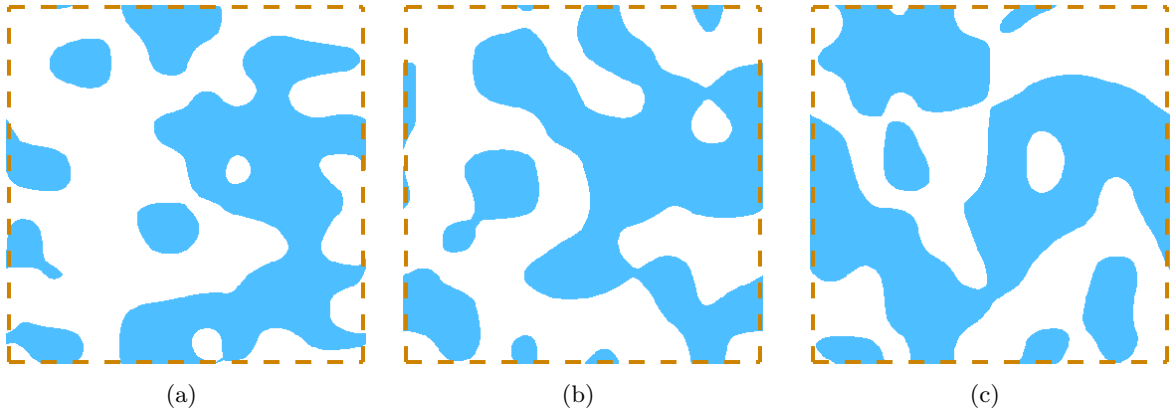


Figure 3: Three random domains generated with a 10x10 quadratic level-set.

every boundary of the RVE. A straightforward way to check whether this condition is fulfilled is therefore to duplicate the RVE in both the  $x$  and  $y$  directions, and just count the groups therein. Fig. 5 illustrates this requirement in three disconnected structures (i.e. an isolated group of material, horizontal or vertical domains in Figs. 5a-c), and a connected one (Fig. 5d).

## 4 Optimization with genetic algorithms

Following classical piezoelectricity (Ikeda, 1996) and the approach used by Mocci et al. (2021), we define four apparent piezoelectric coupling coefficients of our metamaterials depending on the electromechanical ensemble:

$$\bar{h} = -\frac{\partial \bar{E}_y}{\partial \bar{\varepsilon}_{yy}} \Big|_{\bar{D}_y=0}, \quad \bar{d} = \frac{\partial \bar{\varepsilon}_{yy}}{\partial \bar{E}_y} \Big|_{\bar{\sigma}_{yy}=0}, \quad \bar{g} = -\frac{\partial \bar{E}_y}{\partial \bar{\sigma}_{yy}} \Big|_{\bar{D}_y=0}, \quad \bar{e} = -\frac{\partial \bar{\sigma}_{yy}}{\partial \bar{E}_y} \Big|_{\bar{\varepsilon}_{yy}=0}, \quad (16)$$

being  $\bar{h}$  and  $\bar{g}$  pertinent to a sensing scenario and  $\bar{d}$  and  $\bar{e}$  to an actuation one. If we refer to one of the aforementioned coefficients as  $\bar{c}$ , the optimization problem can be stated as:

$$\begin{aligned} \min_{\boldsymbol{\Phi}} \quad & -|\bar{c}(\boldsymbol{\Phi})|, \\ \text{subject to:} \quad & A_f(\boldsymbol{\Phi}) \leq A_{\max}, \\ & N_g(\boldsymbol{\Phi}) = 1, \end{aligned} \quad (17)$$

where  $\boldsymbol{\Phi}$  is the vector of control points of the level set function describing the domain,  $A_f(\boldsymbol{\Phi}) = |\Omega(\boldsymbol{\Phi})|/|\Omega^{\text{RVE}}|$  is the area fraction of the structure, which is normally set to be smaller than a given fraction  $A_{\max}$ , and  $N_g(\boldsymbol{\Phi})$  is the number of groups defined in the previous section. The absolute value  $|\bar{c}(\boldsymbol{\Phi})|$  is introduced to account for those configurations that, according to the definition given by Eq. (16), would have a negative coefficient but whose shape is still valid for the optimization purpose.

As far as the numerical implementation is concerned, we use the MATLAB<sup>®</sup> genetic algorithm toolbox (Chipperfield and Fleming, 1995). However, we note that in feeding the optimization problem stated in Eq. (17) directly to the solver, the optimization procedure fails in most of the cases, since the initial randomly generated population in general does not verify both constraints,

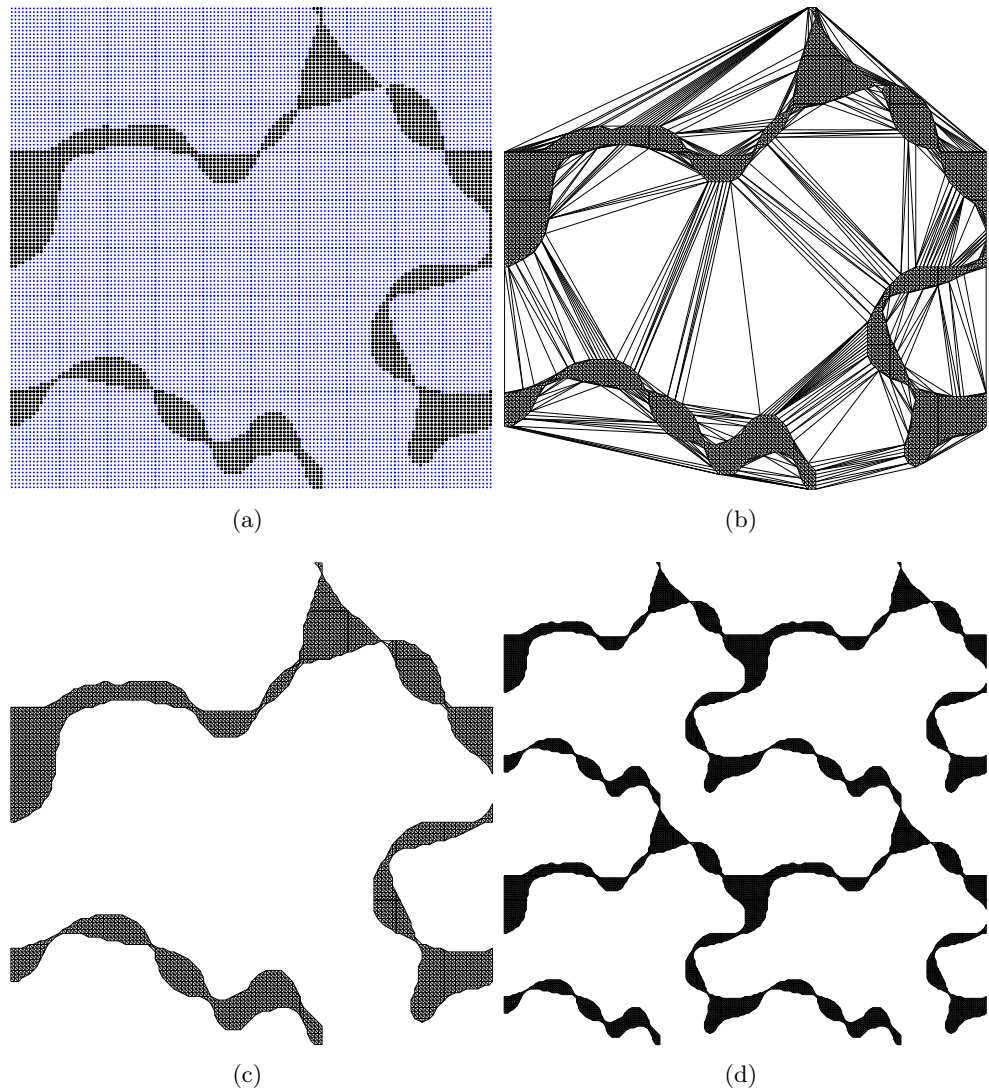


Figure 4: The procedure used to determine the number of groups. The domain is first sampled with a cloud of points and the ones with  $\Phi(\mathbf{x})$  (in black) are maintained (a); then the Delaunay triangulation is computed (b); the alpha-shape is extracted (c); and the domain is duplicated to count the number of groups (d). Note that for the purpose of this illustration, a low number of sampling points and a slightly higher value of  $\alpha$  have been used.

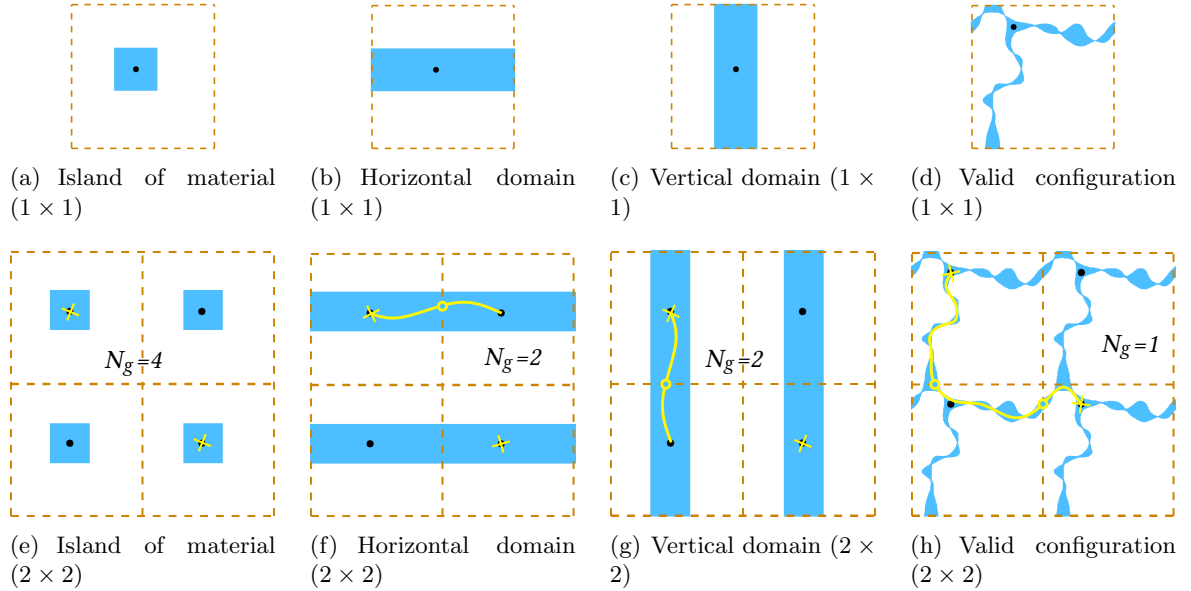


Figure 5: Four different configurations in a single  $(1 \times 1)$  and replicated  $(2 \times 2)$  RVE. While  $N_g = 1$  in the single RVE for all cases,  $N_g$  in the replicated RVE might differ. Only in the valid configuration of (d) and (h) it is possible to create a path (yellow line) between each point in the domain and an image of itself in the opposite RVE (yellow crosses), while intersecting every RVE boundary (yellow circles).

and then the algorithm converges to infeasible local minima either if a penalty or an augmented Lagrangian formulation is used. We therefore resort to a more effective strategy, which consists in solving a multi-objective problem, where both the apparent piezoelectric coefficient and the area fraction are optimized:

$$\begin{aligned} \min_{\boldsymbol{\Phi}} \quad & -|\bar{c}(\boldsymbol{\Phi})|, A_f(\boldsymbol{\Phi}), \\ \text{subject to: } \quad & N_g(\boldsymbol{\Phi}) = 1. \end{aligned} \quad (18)$$

This approach is not only more efficient from a numerical point of view but also more useful to understand the physics of the problem and how the different coefficients depend on the area fraction. A detailed discussion on this topic follows in the next section.

Also in the case of the Pareto formulation stated by Eq. (18), we note that if a randomly generated initial population is used the algorithm often converges to a set of individuals located on a small fraction of the whole Pareto front. Therefore, the initial population is enriched with a set of individuals computed by solving the modified Pareto problem:

$$\min_{\boldsymbol{\Phi}} \quad -|\bar{c}(\boldsymbol{\Phi})| + \beta A_f(\boldsymbol{\Phi}) + \gamma (N_g(\boldsymbol{\Phi}) - 1)^2, \quad (19)$$

where the Pareto parameter  $\beta$  takes different values in a range that allows us to span the entire Pareto region. In this case, the constraint  $N_g = 1$  is imposed weakly using a penalty approach with a very high coefficient  $\gamma$ , such that even if the optimization starts with infeasible individuals, it progressively prefers those with smaller values of  $N_g$  and gradually converges to valid configurations. In particular, a value of  $\gamma = 10^{20}$  is used.

Table 1: Material parameters used in the multi-objective optimization analyses.

$Y$ [Gpa]	$\nu$	$\ell_{\text{mech}}$ [nm]	$\ell_{\text{elec}}$ [nm]	$\epsilon$ [nC/Vm]	$\mu_L$ [ $\mu\text{C}/\text{m}$ ]	$\mu_T$ [ $\mu\text{C}/\text{m}$ ]	$\mu_S$ [ $\mu\text{C}/\text{m}$ ]
152	0.33	50	300	8	1.21	1.10	0.055

Table 2: Macroscopic conditions for the multi-objective optimization analyses. A value 0 means that this corresponding quantity is constrained to 0, whereas (-) means that the corresponding quantity is a Lagrange multiplier for the constraint that does not participate in the relevant output.

	$\bar{\varepsilon}_{yy}$	$\bar{\sigma}_{yy}$	$E_y$	$D_y$	$\bar{\varepsilon}_{xx}$	$\bar{\sigma}_{xx}$	$\bar{\varepsilon}_{xy}$	$\bar{\sigma}_{xy}$	$E_x$	$D_x$
$\bar{h}$	Input	-	Output	0	0	-	0	-	0	-
$\bar{d}$	Output	0	Input	-	0	-	0	-	0	-
$\bar{g}$	-	Input	Output	0	0	-	0	-	0	-
$\bar{e}$	0	Output	Input	-	0	-	0	-	0	-

## 5 Numerical results and discussion

The multi-objective problem stated in Eq. (18) is solved for the four apparent piezoelectric coefficients introduced in Eq. (16). We consider a square unit cell of size  $4\mu\text{m}$ . The material parameters are summarized in Table 1 and correspond to those of a barium strontium titanate (BST) ferroelectric ceramic. The complete sets of macroscopic conditions are stated in Table 2 for each optimization problem.

The level set description of the domain is given by a  $10 \times 10$  quadratic ( $p = 2$ ) B-spline grid, whose control points are the variables to be optimized. The computational mesh is given by a  $100 \times 100$  cubic ( $p = 3$ ) B-spline grid. The multi-objective optimization problems are solved considering a population of 2000 individuals and 2000 generations. For all the cases, the initial population is enriched with 30 seed individuals computed by solving the problem stated by Eq. (19).

In principle, the interplay between apparent piezoelectricity and area fraction is non-trivial because, on the one hand, higher area fraction uses more material capable of mobilizing flexoelectricity, but on the other hand, slender structures may develop higher field gradients. Figure 6 summarizes the results of the optimization procedure for each of the four device conditions, strain sensor ( $\bar{h}$ ), strain actuator ( $\bar{d}$ ), stress sensor ( $\bar{g}$ ), and stress actuator ( $\bar{e}$ ). In each case, we represent in the plane of objective functions ( $\bar{h}$ ,  $\bar{d}$ ,  $\bar{g}$  or  $\bar{e}$  vs. area fraction  $A_f$ ) the seeds used in the genetic algorithm and the portions of the Pareto front identified by our numerical study. We label with colors branches of the Pareto front characterized by a smooth shape and by similar microstructures. For each device functionality, we plot a pertinent field (electric field, displacement or stress) on representative microstructures.

We first note that our topology optimization algorithm identifies microstructures that share the general features of those proposed heuristically by [Mocci et al. \(2021\)](#), namely geometric polarization and slender elements, except those for stress actuators and higher area fraction, Fig. 6(d), which look more like bulk materials with geometrically polarized inclusions as proposed by [Sharma et al. \(2007\)](#). It is interesting to note that for this case, where a macroscopic electric field is applied and the resulting stress at zero strain recorded, the area fractions of the Pareto

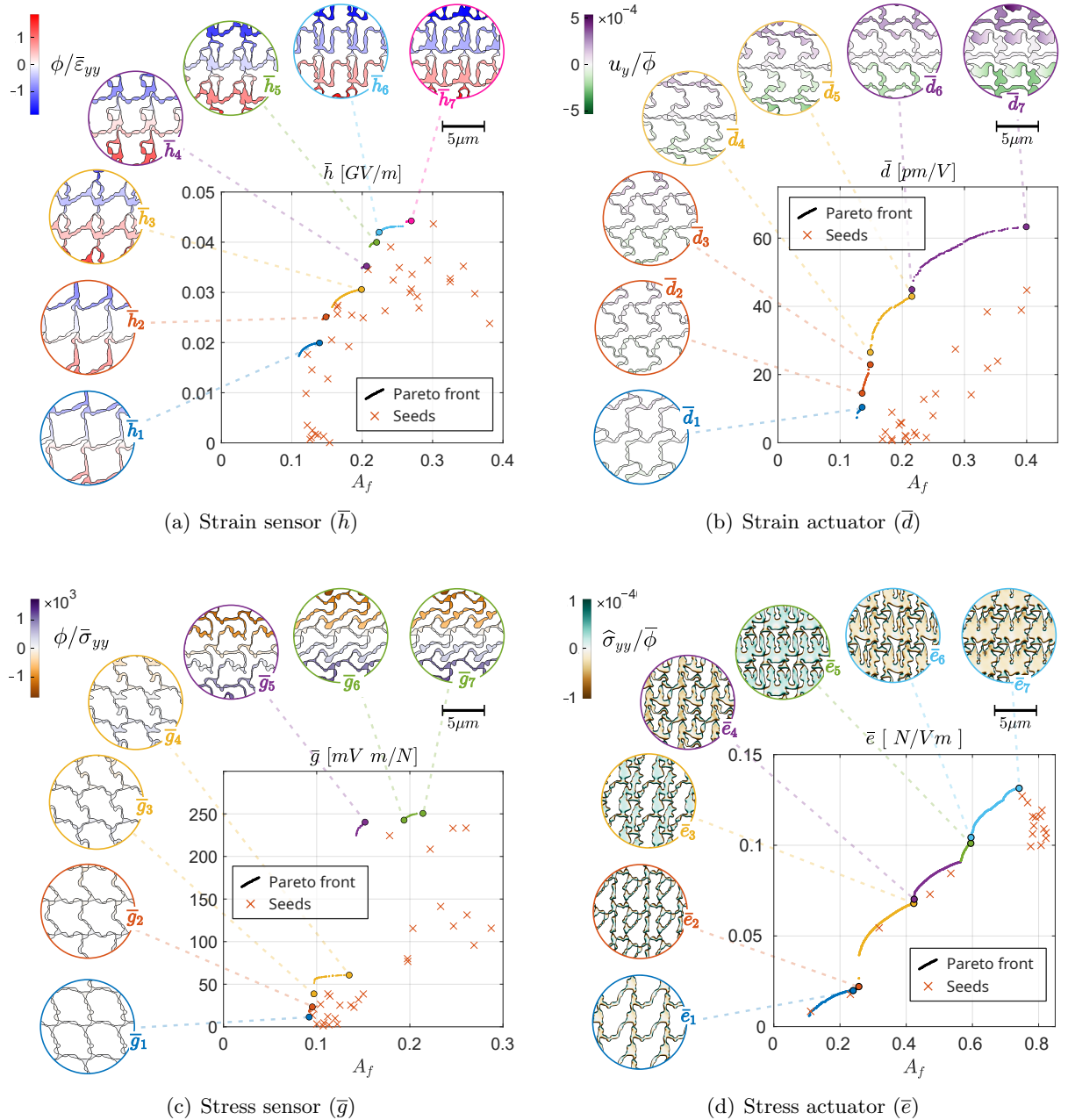


Figure 6: Pareto fronts of the multi-objective optimization problems. Each color represents topologically similar microstructures. The insets show selected microstructures, and their colorbars represent normalized quantities for visualization, i.e. they are normalized with respect to some reference values: the electric potential and macroscopic potential drop are divided by  $\mu_L/\kappa$ , the displacement is divided by  $L_y$ , and the microscopic Cauchy stress and macroscopic stress are divided by  $Y$ .

Table 3: Reference values for piezoelectric coefficients in Quartz and PZT ceramics, compared to the largest apparent piezoelectric coefficients of the microstructures found in this work.

	$\bar{h}$ [GV/m]	$\bar{d}$ [pm/V]	$\bar{g}$ [mV m/N]	$\bar{e}$ [N/Vm]
Quartz ( <a href="#">Kholkin et al., 2008</a> )	5	2.3	50	0.23
PZT ( <a href="#">Kholkin et al., 2008</a> )	1.4	280	25	20.23
Architected material	0.04 ( $\bar{h}_7$ )	63 ( $\bar{d}_7$ )	250 ( $\bar{g}_7$ )	0.13 ( $\bar{e}_7$ )

front span a wide range from 0.1 to close to 0.8. For this functionality, it is clear that more material leads to higher stiffness and can produce a higher stress, but on the other hand an area fraction close to 1 approaches a centrosymmetric bulk material with vanishing apparent piezoelectricity. In all other cases, this range is much narrower and below 0.4, suggesting that for many applications optimal performance is achieved at reduced area fraction. For the strain actuator  $\bar{d}$ , Fig. 6(b), under an applied electric field the output is the vertical strain at zero stress. Accordingly, the optimized structures look like scissor mechanisms with non-centrosymmetric sub-units. While here it is unclear whether more material can increase strain actuation, we find in the larger area-fraction branches that increasing feature thickness with similar microstructure shape improves performance, (branches  $\bar{d}_2$  to  $\bar{d}_3$  or  $\bar{d}_4$  to  $\bar{d}_5$ ).

Turning to sensor configurations, the goal is to maximize the macroscopic electric field for a given applied macroscopic strain ( $\bar{h}$ ) or stress ( $\bar{g}$ ). Intuitively, we expect stress sensors to be very compliant along the  $y$  direction to maximize mechanical gradients under a given stress and hence produce a strong flexoelectric response. Accordingly, we obtain apparently floppy structures with horizontally arranged  $S$ -shaped elements, Fig. 6(c). In contrast, strain sensors appear stiffer and exhibit vertically arranged elements, which produce higher flexoelectric coupling at fixed applied strain, Fig. 6(a).

A quantitative comparison with reference values for piezoelectric coefficients of Quartz and PZT ceramics ([Kholkin et al., 2008](#)), reported in Table 3, shows that the apparent piezoelectric coefficients found in this study are higher than those of Quartz and PZT for the case of  $\bar{g}$ , and in the same range for the case of  $\bar{d}$ . The values found for  $\bar{e}$  are competitive only with respect to Quartz, while for  $\bar{h}$  our metamaterials are significantly less performant than the reference piezoelectric materials. We should note that the piezoelectric properties reported in the table are in absolute terms. When normalized by mass or area fraction, they are much more favorable to our metamaterials. Furthermore, metamaterials with apparent piezoelectricity can in principle be manufactured from any dielectric, can be lead-free and rather insensitive to temperature as opposed to PZT. It is also true that for all four apparent piezoelectric responses, the lowest area fractions may lead to excessively compliant structures. Furthermore, our optimization framework has not considered fabrication constraints ([Zegard and Paulino, 2016](#)) nor limited maximum stresses ([da Silva et al., 2021](#)), strains or electric field, which may result in material damage or electric breakdown.

## 6 Concluding remarks

We have presented a theoretical and computational framework for the two dimensional topology optimization of flexoelectric metamaterials with apparent piezoelectricity. Different actuator

and sensor functionalities have been optimized, finding numerical approximations of the Pareto fronts with respect to such piezoelectric responses and area minimization. Interestingly, our optimization procedure recovers and improves the kind of metamaterial RVEs proposed by [Mocci et al. \(2021\)](#) on the basis of physical reasoning. Using a good flexoelectric material as base material (BST) for our metamaterials, we obtain apparent piezoelectric coefficients  $\bar{h}$ ,  $\bar{d}$ ,  $\bar{g}$  and  $\bar{e}$  that are competitive with respect to the reference Quartz and PZT values, illustrating that flexoelectric structures can provide significant apparent piezoelectricity from a much wider and cheaper range of materials. A reference size of  $4\mu\text{m}$  has been considered for the unit cell but, as shown by previous studies, the apparent piezoelectric coefficients can be improved by working at a smaller scale due to the size dependency flexoelectricity. The topology of the optimized structures provide useful insight on how the microscopic flexoelectric behavior is leveraged for each distinct piezoelectric functionality, which can inspire simpler and more manufacturable structures. Finally, a significant improvement is expected by 3D optimization of flexoelectric metamaterials, the topic of future research.

## Acknowledgements

This work was supported by the European Research Council (StG-679451 to I.A.), the Spanish Ministry of Economy and Competitiveness (RTI2018-101662-B-I00) and through the “Severo Ochoa Programme for Centres of Excellence in R&D” (CEX2018-000797-S), and the Generalitat de Catalunya (ICREA Academia award for excellence in research to I.A., and Grant No. 2017-SGR-1278). D.C. acknowledges the support of the Spanish Ministry of Universities through the Margarita Salas fellowship (European Union-NextGenerationEU).

## CRediT authorship contribution statement

**F. Greco:** Conceptualization, Methodology, Software, Validation, Formal analysis, Data curation, Visualization, Writing – original draft. **D. Codony:** Conceptualization, Methodology, Software, Validation, Formal analysis, Data curation, Visualization, Writing – original draft. **H. Mohammadi:** Conceptualization, Methodology, Writing – original draft. **S. Fernandez:** Conceptualization, Methodology, Supervision. **I. Arias:** Conceptualization, Methodology, Supervision, Writing – review and editing, Resources, Project administration, Funding acquisition.

## References

Amir Abdollahi, Christian Peco, Daniel Millan, Marino Arroyo, and Irene Arias. Computational evaluation of the flexoelectric effect in dielectric solids. *Journal of Applied Physics*, 116(9): 93502, 2014. URL <https://doi.org/10.1063/1.4893974>.

Nataraj Akkiraju, Herbert Edelsbrunner, Michael Facello, Ping Fu, EP Mucke, and Carlos Varela. Alpha shapes: definition and software. In *Proceedings of the 1st international computational geometry software workshop*, pages 63–66, 1995.

Oscar Balcells-Quintana, David Codony, and Sonia Fernández-Méndez. C0-IPM with generalised periodicity and application to flexoelectricity-based 2D metamaterials. *Journal of Scientific Computing*, 92(1):1–29, 2022. URL <https://doi.org/10.1007/s10915-022-01848-1>.

Jordi Barceló-Mercader, David Codony, Sonia Fernández-Méndez, and Irene Arias. Weak enforcement of interface continuity and generalized periodicity in high-order electromechanical problems. *International Journal for Numerical Methods in Engineering*, 123(4):901–923, 2022. URL <https://doi.org/10.1002/nme.6882>.

Jordi Barceló-Mercader, Alice Mocci, David Codony, and Irene Arias. High-order generalized periodicity conditions for architected materials with application to flexoelectricity. *In preparation*, 2023.

AJ Chipperfield and PJ Fleming. *The MATLAB genetic algorithm toolbox*, 1995. URL <https://doi.org/10.1049/ic:19950061>.

D Codony, Alice Mocci, Jordi Barceló-Mercader, and I Arias. Mathematical and computational modeling of flexoelectricity. *Journal of Applied Physics*, 130(23):231102, 2021. URL <https://doi.org/10.1063/5.0067852>.

David Codony, Onofre Marco, Sonia Fernández-Méndez, and Irene Arias. An Immersed Boundary Hierarchical B-spline method for flexoelectricity. *Computer Methods in Applied Mechanics and Engineering*, 2019. URL <https://doi.org/10.1016/j.cma.2019.05.036>.

David Codony, Prakhar Gupta, Onofre Marco, and Irene Arias. Modeling flexoelectricity in soft dielectrics at finite deformation. *Journal of the Mechanics and Physics of Solids*, page 104182, 2020. URL <https://doi.org/10.1016/j.jmps.2020.104182>.

CA Coello and Alan D Christiansen. Multiobjective optimization of trusses using genetic algorithms. *Computers & Structures*, 75(6):647–660, 2000. URL [https://doi.org/10.1016/S0045-7949\(99\)00110-8](https://doi.org/10.1016/S0045-7949(99)00110-8).

Gustavo Assis da Silva, Niels Aage, André Teófilo Beck, and Ole Sigmund. Local versus global stress constraint strategies in topology optimization: A comparative study. *International Journal for Numerical Methods in Engineering*, 122(21):6003–6036, jul 2021. doi: 10.1002/nme.6781. URL <https://doi.org/10.1002%2Fnme.6781>.

C. de Boor. *A Practical Guide to Splines*. Applied Mathematical Sciences. Springer New York, 2001. ISBN 9780387953663. URL <http://www.springer.com/gb/book/9780387953663>.

Feng Deng, Qian Deng, Wenshan Yu, and Shengping Shen. Mixed finite elements for flexoelectric solids. *Journal of Applied Mechanics*, 84(8):81004, 2017. URL <https://doi.org/10.1115/1.4036939>.

Hien V Do, T Lahmer, X Zhuang, N Alajlan, H Nguyen-Xuan, and Timon Rabczuk. An isogeometric analysis to identify the full flexoelectric complex material properties based on electrical impedance curve. *Computers & Structures*, 214:1–14, 2019. URL <https://doi.org/10.1016/j.compstruc.2018.10.019>.

Fuat Erbatur, Oğuzhan Hasançebi, İlker Tütüncü, and Hakan Kılıç. Optimal design of planar and space structures with genetic algorithms. *Computers & Structures*, 75(2):209–224, 2000. URL [https://doi.org/10.1016/S0045-7949\(99\)00084-X](https://doi.org/10.1016/S0045-7949(99)00084-X).

Alper Erturk and Daniel J Inman. *Piezoelectric energy harvesting*. John Wiley & Sons, 2011. URL <https://doi.org/10.1002/9781119991151>.

J Fousek, L E Cross, and D B Litvin. Possible piezoelectric composites based on the flexoelectric effect. *Materials Letters*, 39(5):287–291, 1999. ISSN 0167-577X. doi: 10.1016/S0167-577X(99)00020-8. URL [http://dx.doi.org/10.1016/S0167-577X\(99\)00020-8](http://dx.doi.org/10.1016/S0167-577X(99)00020-8).

Xiangyu Gao, Jikun Yang, Jingen Wu, Xudong Xin, Zhanmiao Li, Xiaoting Yuan, Xinyi Shen, and Shuxiang Dong. Piezoelectric actuators and motors: materials, designs, and applications. *Advanced Materials Technologies*, 5(1):1900716, 2020. URL <https://doi.org/10.1002/admt.201900716>.

Gustav Gautschi. *Piezoelectric Sensorics: Force Strain Pressure Acceleration and Acoustic Emission Sensors Materials and Amplifiers*. Springer Science & Business Media, 2006. URL <https://www.osti.gov/etdeweb/biblio/20283117>.

Hamid Ghasemi, Harold S Park, and Timon Rabczuk. A level-set based IGA formulation for topology optimization of flexoelectric materials. *Computer Methods in Applied Mechanics and Engineering*, 313:239–258, 2017. URL <https://doi.org/10.1016/j.cma.2016.09.029>.

Hamid Ghasemi, Harold S Park, and Timon Rabczuk. A multi-material level set-based topology optimization of flexoelectric composites. *Computer Methods in Applied Mechanics and Engineering*, 332:47–62, 2018. URL <https://doi.org/10.1016/j.cma.2017.12.005>.

Gene H Haertling. Ferroelectric ceramics: history and technology. *Journal of the American Ceramic Society*, 82(4):797–818, 1999. URL <https://doi.org/10.1111/j.1151-2916.1999.tb01840.x>.

Prabhat Hajela and E Lee. Genetic algorithms in truss topological optimization. *International journal of solids and structures*, 32(22):3341–3357, 1995. URL [https://doi.org/10.1016/0020-7683\(94\)00306-H](https://doi.org/10.1016/0020-7683(94)00306-H).

Khader M Hamdia, Hamid Ghasemi, Yakoub Bazi, Haikel AlHichri, Naif Alajlan, and Timon Rabczuk. A novel deep learning based method for the computational material design of flexoelectric nanostructures with topology optimization. *Finite Elements in Analysis and Design*, 165:21–30, 2019. URL <https://doi.org/10.1016/j.finel.2019.07.001>.

Khader M Hamdia, Hamid Ghasemi, Xiaoying Zhuang, and Timon Rabczuk. Multilevel monte carlo method for topology optimization of flexoelectric composites with uncertain material properties. *Engineering Analysis with Boundary Elements*, 134:412–418, 2022. URL <https://doi.org/10.1016/j.enganabound.2021.10.008>.

Klaus Höllig, Ulrich Reif, and Joachim Wipper. Weighted extended b-spline approximation of dirichlet problems. *SIAM Journal on Numerical Analysis*, 39(2):442–462, 2001. URL <https://doi.org/10.1137/S0036142900373208>.

Chang-Hyo Hong, Hwang-Pill Kim, Byung-Yul Choi, Hyoung-Su Han, Jae Sung Son, Chang Won Ahn, and Wook Jo. Lead-free piezoceramics—Where to move on? *J. Materomics*, 2(1):1–24, 2016. URL <https://doi.org/10.1016/j.jmat.2015.12.002>.

Takurō Ikeda. *Fundamentals of piezoelectricity*. Oxford university press, 1996.

Chang-Hwan Im, Hyun-Kyo Jung, and Yong-Joo Kim. Hybrid genetic algorithm for electromagnetic topology optimization. *IEEE Transactions on Magnetics*, 39(5):2163–2169, 2003. URL <https://doi.org/10.1109/TMAG.2003.817094>.

WM Jenkins. Towards structural optimization via the genetic algorithm. *Computers & Structures*, 40(5):1321–1327, 1991. URL [https://doi.org/10.1016/0045-7949\(91\)90402-8](https://doi.org/10.1016/0045-7949(91)90402-8).

Xiaoning Jiang, Wenbin Huang, and Shujun Zhang. Flexoelectric nano-generator: Materials, structures and devices. *Nano Energy*, 2(6):1079–1092, 2013. URL <https://doi.org/10.1016/j.nanoen.2013.09.001>.

AL Kholkin, DA Kiselev, LA Khokhine, and Ahmad Safari. Piezoelectric and electrostrictive ceramics transducers and actuators: Smart ferroelectric ceramics for transducer applications. In *Smart Materials*, pages 9–1. CRC Press, 2008.

Chang Liu, Jie Wang, Gang Xu, Marc Kamlah, and Tong-Yi Zhang. An isogeometric approach to flexoelectric effect in ferroelectric materials. *International Journal of Solids and Structures*, 162:198–210, 2019. URL <https://doi.org/10.1016/j.ijsolstr.2018.12.008>.

Jorge López, Navid Valizadeh, and Timon Rabczuk. An isogeometric phase–field based shape and topology optimization for flexoelectric structures. *Computer Methods in Applied Mechanics and Engineering*, 391:114564, 2022. URL <https://doi.org/10.1016/j.cma.2021.114564>.

Sheng Mao, Prashant K Purohit, and Nikolaos Aravas. Mixed finite-element formulations in piezoelectricity and flexoelectricity. *Proceedings of the Royal Society A: Mathematical, Physical and Engineering Sciences*, 472(2190):20150879, 2016. URL <https://doi.org/10.1098/rspa.2015.0879>.

Richard M Martin. Piezoelectricity. *Physical Review B*, 5(4):1607, 1972. URL <https://doi.org/10.1103/PhysRevB.5.1607>.

Alice Mocci, Jordi Barceló-Mercader, D Codony, and I Arias. Geometrically polarized architected dielectrics with apparent piezoelectricity. *Journal of the Mechanics and Physics of Solids*, 157:104643, 2021. URL <https://doi.org/10.1016/j.jmps.2021.104643>.

Paul Muralt. Recent progress in materials issues for piezoelectric MEMS. *Journal of the American Ceramic Society*, 91(5):1385–1396, 2008. URL <https://doi.org/10.1111/j.1551-2916.2008.02421.x>.

SS Nanthakumar, Xiaoying Zhuang, Harold S Park, and Timon Rabczuk. Topology optimization of flexoelectric structures. *Journal of the Mechanics and Physics of Solids*, 105:217–234, 2017. URL <https://doi.org/10.1016/j.jmps.2017.05.010>.

Thanh D Nguyen, Sheng Mao, Yao-Wen Yeh, Prashant K Purohit, and Michael C McAlpine. Nanoscale Flexoelectricity. *Advanced Materials*, 25(7):946–974, 2013. doi: 10.1002/adma.201203852. URL <https://onlinelibrary.wiley.com/doi/abs/10.1002/adma.201203852>.

L. Piegl and W. Tiller. *The NURBS Book*. Monographs in Visual Communication. Springer Berlin Heidelberg, 2012. ISBN 9783642973857. doi: 10.1007/978-3-642-97385-7. URL <https://doi.org/10.1007/978-3-642-97385-7>.

Ernst Rank, Martin Ruess, Stefan Kollmannsberger, Dominik Schillinger, and Alexander Düster. Geometric modeling, isogeometric analysis and the finite cell method. *Computer Methods in Applied Mechanics and Engineering*, 249:104–115, 2012. URL <https://doi.org/10.1016/j.cma.2012.05.022>.

Jürgen Rödel, Wook Jo, Klaus T P Seifert, Eva-Maria Anton, Torsten Granzow, and Dragan Damjanovic. Perspective on the development of lead-free piezoceramics. *J. Am. Ceram. Soc.*, 92(6):1153–1177, 2009. URL <https://doi.org/10.1111/j.1551-2916.2009.03061.x>.

D.F. Rogers. *An Introduction to NURBS: With Historical Perspective*. Morgan Kaufmann Series in Computer Graphics and Geometric Modeling. Morgan Kaufmann Publishers, 2001. ISBN 9781558606692. URL <https://doi.org/10.1016/B978-1-55860-669-2.X5000-3>.

Mohsen Safaei, Henry A Sodano, and Steven R Anton. A review of energy harvesting using piezoelectric materials: state-of-the-art a decade later (2008–2018). *Smart Materials and Structures*, 28(11):113001, 2019. URL <https://doi.org/10.1088/1361-665X/ab36e4>.

Yasuyoshi Saito, Hisaaki Takao, Toshihiko Tani, Tatsuhiko Nonoyama, Kazumasa Takatori, Takahiko Homma, Toshiatsu Nagaya, and Masaya Nakamura. Lead-free piezoceramics. *Nature*, 432(7013):84–87, 2004. URL <https://doi.org/10.1038/nature03028>.

N D Sharma, Ravi Maranganti, and P Sharma. On the possibility of piezoelectric nanocomposites without using piezoelectric materials. *Journal of the Mechanics and Physics of Solids*, 55(11):2328–2350, 2007. URL <https://doi.org/10.1016/j.jmps.2007.03.016>.

Saurav Sharma, Anuruddh Kumar, Rajeev Kumar, Mohammad Talha, and Rahul Vaish. Geometry independent direct and converse flexoelectric effects in functionally graded dielectrics: an isogeometric analysis. *Mechanics of Materials*, 148:103456, 2020. URL <https://doi.org/10.1016/j.mechmat.2020.103456>.

Nipun Sinha, Graham E Wabiszewski, Rashed Mahameed, Valery V Felmetser, Shawn M Tanner, Robert W Carpick, and Gianluca Piazza. Piezoelectric aluminum nitride nanoelectromechanical actuators. *Applied Physics Letters*, 95(5):053106, 2009. URL <https://doi.org/10.1063/1.3194148>.

Gabriel L Smith, Jeffrey S Pulskamp, Luz M Sanchez, Daniel M Potrepka, Robert M Proie, Tony G Ivanov, Ryan Q Rudy, William D Nothwang, Sarah S Bedair, Christopher D Meyer, et al. PZT-based piezoelectric MEMS technology. *Journal of the American Ceramic Society*, 95(6):1777–1792, 2012. URL <https://doi.org/10.1111/j.1551-2916.2012.05155.x>.

Robert Tarjan. Depth-first search and linear graph algorithms. *SIAM journal on computing*, 1(2):146–160, 1972. URL <https://doi.org/10.1137/0201010>.

Tran Quoc Thai, Timon Rabczuk, and Xiaoying Zhuang. A large deformation isogeometric approach for flexoelectricity and soft materials. *Computer Methods in Applied Mechanics and Engineering*, 341:718–739, 2018. URL <https://doi.org/10.1016/j.cma.2018.05.019>.

Marco Tomassini. A survey of genetic algorithms. *Annual reviews of computational physics III*, pages 87–118, 1995. URL [https://doi.org/10.1142/9789812830647\\_0003](https://doi.org/10.1142/9789812830647_0003).

James F Tressler, Sedat Alkoy, and Robert E Newnham. Piezoelectric sensors and sensor materials. *Journal of electroceramics*, 2(4):257–272, 1998. URL <https://doi.org/10.1023/A:1009926623551>.

Jordi Ventura, David Codony, and Sonia Fernández-Méndez. A C0 interior penalty finite element method for flexoelectricity. *Journal of Scientific Computing*, 88(88), 2021. URL <https://doi.org/10.1007/s10915-021-01613-w>.

Bo Wang, Yijia Gu, Shujun Zhang, and Long-Qing Chen. Flexoelectricity in solids: Progress, challenges, and perspectives. *Progress in Materials Science*, 106:100570, 2019a. ISSN 0079-6425. doi: <https://doi.org/10.1016/j.pmatsci.2019.05.003>. URL <http://www.sciencedirect.com/science/article/pii/S0079642519300465>.

Bo Wang, Yijia Gu, Shujun Zhang, and Long-Qing Chen. Flexoelectricity in solids: Progress, challenges, and perspectives. *Progress in Materials Science*, 106:100570, 2019b. URL <https://doi.org/10.1016/j.pmatsci.2019.05.003>.

Julien Yvonnet and L P Liu. A numerical framework for modeling flexoelectricity and Maxwell stress in soft dielectrics at finite strains. *Computer Methods in Applied Mechanics and Engineering*, 313:450–482, 2017. URL <https://doi.org/10.1016/j.cma.2016.09.007>.

Tomás Zegard and Glaucio H. Paulino. Bridging topology optimization and additive manufacturing. *Structural and Multidisciplinary Optimization*, 53(175–192), 2016. URL <https://doi.org/10.1007/s00158-015-1274-4>.

Weisheng Zhang, Xiaoye Yan, Yao Meng, Chunli Zhang, Sung-Kie Youn, and Xu Guo. Flexoelectric nanostructure design using explicit topology optimization. *Computer Methods in Applied Mechanics and Engineering*, 394:114943, 2022. URL <https://doi.org/10.1016/j.cma.2022.114943>.

Xiaoying Zhuang, SS Nanthakumar, and Timon Rabczuk. A meshfree formulation for large deformation analysis of flexoelectric structures accounting for the surface effects. *Engineering Analysis with Boundary Elements*, 120:153–165, 2020. URL <https://doi.org/10.1016/j.enganabound.2020.07.021>.

Pavlo Zubko, Gustau Catalan, and Alexander K Tagantsev. Flexoelectric effect in solids. *Annual Review of Materials Research*, 43, 2013. URL <https://doi.org/10.1146/annurev-matsci-071312-121634>.